Inverse Problems in the MEMS/NEMS Applications

Yin Zhang*

State Laboratory of Nonlinear Mechanics, Institute of Mechanics, Chinese Academy of Sciences, Beijing, China

Abstract

As a structure is scaled down, the ratio of surface to volume increases and the surface effects thus stand out, which may result in the different material properties from those of bulk. Therefore, some key parameters such as Young's modulus and adhesion energy, which concern the performance and reliability of the micro/nano-electro-mechanical systems (MEMS/NEMS), are unknown. Sometimes, the direct measurements of some parameters are extremely difficult if not impossible, for example, measuring the position of an adsorbate as small as a molecule or an atom. How to use the measured quantities such as resonant frequencies and deformation to determine those key parameters forms an inverse problem. Every inverse problem requires a particular approach. In this chapter, we present some effective approaches of solving the inverse problems in the MEMS/NEMS applications. The chapter consists of two major parts: the inverse problems in (1) micro/nano mechanical resonator and (2) the stiction test of MEMS/NEMS.

Keywords: Inverse problem, MEMS/NEMS, resonator, sensor, stiction

7.1 Introduction

"*Most mathematical problems in science, technology and medicine are inverse problems*" [1]. For example, in geophysics and medicine, the inverse problem arises as the determination of properties of some inaccessible regions from the observations on the boundary of those regions [1]. In the applications of MEMS/NEMS, many physical parameters are not subject to direct measurements and the effects induced by these parameters are then the only measurable quantities.

Solving the inverse problems is to relate the (measured) effects with those (intrinsic) physical parameters. For practical applications, the interpretation of experimental findings is of fundamental importance and studying inverse problems is the only complete way of analyzing experimental results [1]. Because the micro/nanomechanical sensor can provide a label-free, high-throughput, and rapid detection of biological and


Corresponding author: zhangyin@lnm.imech.ac.cn

chemical molecules [2,3], it has become increasingly important in detecting tiny force or mass [4–8]. Depending on the nature of the input stimuli, micromechanical sensor can be categorized as physical, chemical, or biological sensor [7].

The adsorbed analytes on a micromechanical sensor surface can cause the changes of mass, damping, stiffness changes and surface stress, etc. [7,8]. These changes can result in the deflection and resonant frequency shifts of a micromechanical sensor, which are also the mechanisms used for sensing. For example, the self-assembly of alkanethiols [5] and the ligand-receptor binding [6] on a microcantilever surface can induce surface stress, which bends the beam. The bending of beam can be related with the surface stress by the following Stoney formula:

$$\Delta\sigma = \frac{Eh^2}{6R(1-\upsilon)} \tag{7.1}$$

where E, υ, and h are the microcantilever Young's modulus, Poisson's ratio, and thickness, respectively. $R = 2L^2 / (3\Delta x)$ is the radius of curvature (L and Δx are the microcantilever length and deflection at the free end as shown in Figure 7.1). $\Delta\sigma$ is the differential surface stress, which has the unit of Nm^{-1} rather than pascal. Here, Δx is the measured quantity, which determines the surface stress ($\Delta\sigma$) by Eq. (7.1). The ligand-receptor binding is highly selectively [6,9], $\Delta\sigma$ can thus be used as an effective criterion to determine what a ligand material is in Fritz's experiment [6].

In the earlier applications of micromechanical sensor using surface stress as the sensing mechanism, surface stress $\Delta\sigma$ has the one-to-one relation with the measured quantity Δx. In general, such one-to-one relation does not hold in many micromechanical sensor
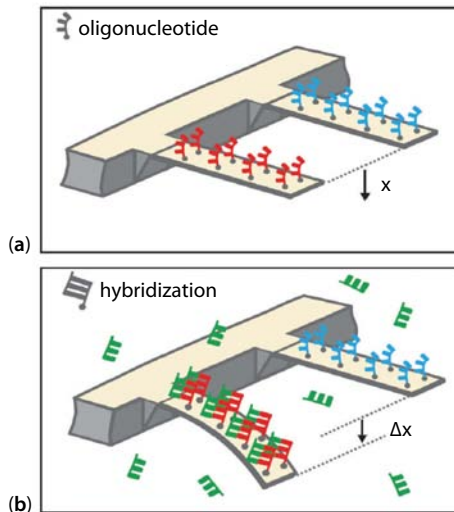
Figure 7.1 Scheme illustrating the hybridization experiment. A different oligonucleotide base sequence (red or blue) is immobilized on one side of cantilever as the receptor materials. (a) The differential signal is set to zero. (b) After injection of the first complementary oligonucleotide (green) as the ligand material, hybridization (ligand-receptor binding) occurs on the cantilever that provides the matching sequence (red), increasing the differential signal of the cantilever free end displacement (Δx). Adapted from Ref. [6].

applications. As mentioned earlier, the mass, damping, and stiffness of sensor change when adsorption occurs. The system resonant frequency changes as follows [4,7]:

$$f' = \frac{1}{2\pi}\sqrt{\frac{K+\Delta K}{M+\Delta M}}\sqrt{1-\frac{(C+\Delta C)^2}{4MK}} \tag{7.2}$$

Where f' is the resonant frequency after adsorption. K, M, and C are the effective spring stiffness, mass, and damping of a micromechanical sensor, respectively. ΔK, ΔM, and ΔC are those corresponding changes due to adsorption. In the real application, f', K, and M are the (known) measured quantity. As the sensor motion is recorded in an experiment, C and ΔC can also be easily determined from the frequency response curve by the half-power method [10]. ΔK and ΔM are the unknowns to be determined. In the forward problem (or alternatively called the direct problem [1]) in which ΔK, ΔM, and ΔC are given, f' is uniquely determined by Eq. (7.2). However, for a measured/given f', there are infinite combinations of ΔK and ΔM. The intrinsic material properties of adsorbate are embodied in ΔK and ΔM, which induce the effects of the resonant frequency changes. Therefore, a natural inverse problem arises in the application of the micromechanical resonator sensor: *How to use the changes of the resonant frequencies to determine the changes of mass and stiffness induced by adsorbates?* The effective mass (ΔM) changes due to two things: the mass of adsorbate and its position, which are the two convolving factors of determining the shifts of the resonant frequencies [11–13]. The stiffness change ΔK is mainly caused by two mechanisms: the stiffness of adsorbate [14,15] and surface stress [4–6,16,17]. When the adsorbate material vibrates with the micromechanical resonator as a whole, the system behaves as a composite structure [14,15] and the stiffness of adsorbate material always cause the system resonant frequencies to increase. As shown in the adsorption tests of *Escherichia coli* (*E. coli*) bacteria on a silicon resonator by Ramos *et al.* [14,15], the system resonant frequencies increase due to the fact that the adsorbate stiffness effect outweighs its mass effect. As surface stress can be either compressive or tensile [4,16,17], it can either decrease or increase the system resonant frequencies. On the other hand, the mechanism for damping (C) for the micromechanical resonator, which indicates the energy dissipation of the system, is a complex one though it can be measured. Various mechanisms and models have been proposed [18]; a clear physics picture still remains elusive.

Another inverse problem arises in the stiction test of MEMS structure. Stiction is a major failure mechanism for MEMS structures [19–25]. The competition between the adhesive force and the microstructure restoring force determines whether the stiction occurs and how the structure deforms [23]. The presence of residual stress changes the structure stiffness and thus leads to the change of the restoring force. The previous models of arc-shape [20,21] and S-shape [24,25] correspond to the zero residual stress case, which also prescribes the stiction shape. When the residual stress becomes large, arc-shape and S-shape significantly deviate from the actual stiction shape of a slender beam. With the assumed stiction shape of arc and S, suspension length is the only parameter needed to characterize the stiction shape and suspension length can also be used to uniquely determine the adhesion energy. However, there are infinite combinations of residual stress and adhesion energy which can result in the same suspension length. The residual stress and adhesion energy are the two key parameters concerning

the performance and reliability of the MEMS/NEMS devices and the stiction test is such an experiment designed to extract these two parameters. However, the residual stress and adhesion energy are the quantities which are extremely difficult to be measured directly. In a stiction test, the measured quantity is the structure deformation shape. Therefore, the inverse problem arises as follows: *How to use the stiction shape of MEMS/NEMS devices to determine the residual stress and adhesion energy?*

7.2   Inverse Problems in the Micro/Nanomechanical Resonators

7.2.1   Determining the Mass and Position of Adsorbate by Using the Shifts of Resonant Frequencies

For a micro/nanomechanical resonator, the resonance change due to adsorption as given in Eq. (7.2) is the sensing mechanism. The ultimate limit for a micro/nanomechanical resonator sensitivity is imposed by the thermodynamic fluctuation [26,27]. For the mass sensing, the theory proved that the limit is well below a Dalton (1 Dalton ≈ 1.65×10^{-24} g is approximately the mass of a proton), which leaves enough room for the development of the micro/nanomechanical resonator. Based on the NEMS technology, Hanay *et al.* [11] developed the resonator sensor capable of detecting a single protein with the mass of approximately one mega-Dalton. Jensen *et al.* [12] developed a carbon nanotube (CNT)-based mechanical resonator sensor capable of detecting one single gold atom with the mass of approximately 197 Dalton. The sensitivity of the CNT-based resonator has recently been pushed by Chaste *et al.* [13] to achieve the capability of detecting the mass of one Dalton. There are three major approaches to push the sensitivity of a micro/nanomechanical resonator sensor toward its ultimate limit. Because the resonant frequency is proportional to $h/L^2 \times \sqrt{E/\rho}$ (h and L are the resonator thickness and length; E and ρ are the Young's modulus and mass density) [28], the first approach is to scale down the resonator size, which is to make the factor h/L^2 large and at the same time fractional change due to a same adsorbate is also larger in a smaller resonator [29]. The second one is to use the materials with large E/ρ, such as silicon [11], silicon carbide [30], CNT [12,13], and graphene [31]. Both approaches are to increase the resonant frequencies. With very large resonant frequencies, a tiny fractional change in the resonant frequencies is still absolutely large enough to be detected [29]. In 2003, a clamped–clamped beam fabricated by the NEMS-based technology achieved the fundamental resonant frequency of around 1 GHz (10^9 Hz), which is a breakthrough as the mechanical vibration frequency enters the microwave range [30]. The third one is to increase the quality factor of a micro/nanomechanical resonator. Quality factor (Q) indicates the sharpness of resonance, which is inversely proportional to damping and has the approximate relation as follows [28,32]:

$$Q \approx \frac{1.09 f_o}{\Delta f} \tag{7.3}$$

where f_o is the resonant frequency (with no adsorbate) and $\Delta f = f' - f_o$ is its shift. For a given resonant frequency f_o, larger Q means smaller Δf can be detected as clearly indicated by Eq. (7.3). The in-plane tension has been shown to be effective on enhancing

quality factor by both simulation [33] and experiment [34]. At the same time, it is always effective to increase quality factor by setting the resonator in a vacuum environment, which reduces or even eliminates the damping due to ambient air [35].

The ultimate goal of any detection method is to achieve the level of resolving a single quantum of a measured entity [36]. For the micro/nanomechanical resonator sensor, the progresses toward this goal are clearly indicated by the improvement of the sensitivity. The resonator sensors with the capability of detecting the presence of a biomolecule [3], a protein [11], a cell [37], a virus [38], a gold atom [12], and a proton [13], have been developed. Although those achievements are very impressive, there is a fundamental problem remained in those mass resonators: all those frequency shift measurements actually cannot give the mass of individual atom, molecule, or nanoparticle [11]. As demonstrated by Jensen *et al.* [12], their CNT-based mass resonator actually does not measure the mass of a gold atom, even though the resonator has the capability of detecting a smaller frequency shift induced by the adsorption of a gold atom. The atom/molecule/particle mass and its position are the two (major) convolving factors of determining the resonant frequency shift of a resonator. To know the position, there are three major experimental approaches: (1) measuring the trajectory of a sprayed particle [26], (2) occluding some portions of resonator so that the particle must land at a specific location [12], and (3) direct measurement of the position of an adsorbate [39]. These measurement approaches not only require extra experimental setup but also (sometimes) are extremely difficult if not impossible to be applied. For example, Dohn *et al.* determined the position of a particle with the size of a micron by using optical image [39]. However, in Burg's resonator with an embedded microfluidic channel where the biomolecules are pumped in [3] as shown in Figure 7.2, the optical method cannot work because the smaller size of a biomolecule and small contrast between a biomolecule and solution. The exact position of the biomolecule is thus a major uncertainty in
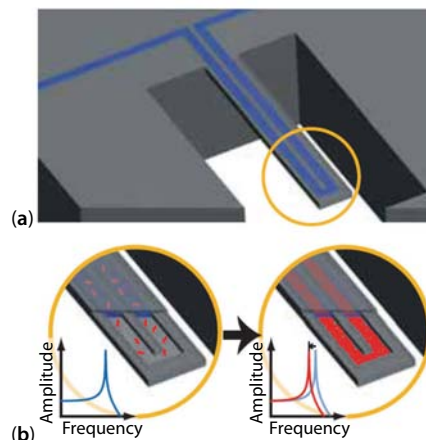

Figure 7.2 Illustration of two mass measurement modes enabled by a fluid-filled microcantilever. (a) The microcantilever is the resonator, and a microfluidic is embedded in the microcantilever. The microchannel translates mass changes into changes in resonance frequency. Fluid continuously flows through the channel and delivers biomolecules, cells, or synthetic particles. (b) Because the biomolecules, cells, or synthetic particles have different mass densities with that of solution, the resonant frequency shown as the blue and red lines changes when biomolecules pass through the microchannel. Adapted from Ref. [3].

Burg's experiment [3]. Knobel [29] gave the following comment: before a practical mass spectrometer can be made, the most important problem to be solved is to determine the atom/molecule/particle position.

In the earlier experiments of mass sensing, an inverse problem is encountered: *How to use the measured resonant frequencies to determine the adsorbate mass and position?* The methods of using multiple resonant frequencies to determine the mass and position of a single adsorbate have been developed [11, 40]. However, unlike the method of probability density function [11] or a minimizing procedure which requires at least four resonant frequencies to be measured [40], the author developed a straightforward method to tackle the problem for a circular membrane resonator made of graphene [28]. The inverse problem solved in Ref. [28] is based on the following two mechanisms: (1) the adsorbate mass and position have different impacts on the same resonant frequency; (2) for a circular membrane which has infinite resonant frequencies, the same adsorbate mass and position have different impact on different resonant frequencies [28,39].

7.2.2   Determining the Adsorption-Induced Surface Stress and Mass by Measuring the Shifts of Resonant Frequencies

As indicated by Eq. (7.2), the adsorption can induce (1) the mass addition, which results in ΔM and always reduces the resonant frequencies, and (2) surface stress, which results in ΔK and can either increases or decreases the resonant frequencies [4]. For a given/measured resonant frequency f', there are infinite possible combinations of ΔM and ΔK. One strategy is to find out either ΔM or ΔK first by a different measurement method and then use the dynamic mode to find the other. For example, by measuring the concentration of adsorbed analyte (ΔM is thus found), ΔK can then be found from Eq. (7.2) [16]; or by localizing the adsorption areas at the terminal end of cantilever to minimize the surface stress effect on the spring stiffness, $\Delta K = 0$ can be assumed [41,42], then ΔM can then be found by applying Eq. (7.2). Obviously, the drawback of this strategy is that extra efforts on device and design, which is not trivial at all, are needed. Another strategy is to use the static mode to measure surface stress to find out ΔK first [e.g., by the Stoney formula of Eq. (7.1)] and then use the dynamic mode to find out ΔK [41,43]. While, the problem of this strategy is that adsorption is a dynamic process. The adsorption-induced mass and surface stress vary not only with time [41,44] but also with how they are measured [44]. In chemical sensors, adsorption and desorption of gas molecules often occur at the same time [45]; in biological sensor, the receptor–ligand such as biotin–streptavidin and biotin–avidin also experiences a dynamic process of bonding–debonding due to the competition between the barrier of mechanical energy, dissociation kinetics, and effect of thermal activation [46]. One vivid example on the difference of the static and dynamic modes is that the adsorption of water on the microcantilever coating layer of polymethyl-methacrylate (PMMA) saturates in the static mode, whereas no saturation is observed in the dynamic mode [44]. The reason is that in the dynamic mode, the diffusion of water within the polymer and the dissolution of the polymer occur simultaneously [44]. In other words, the static mode and dynamic mode may not measure the same adsorption-induced mass and surface stress. Ref. [4] presents a general method of
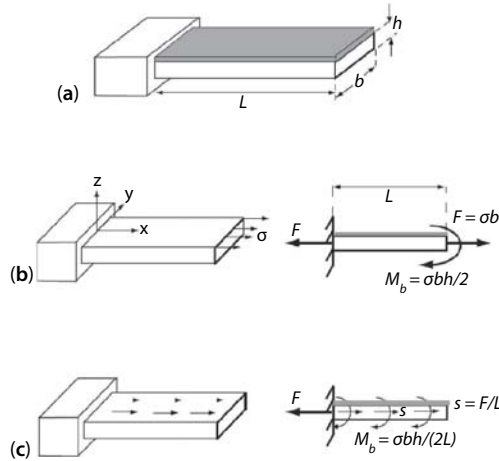
Figure 7.3 (a) Schematic of a cantilever with a uniform layer of adsorption on its upper surface. The cantilever is with the length L, width b, and thickness h. (b) The concentrated load modeling: σ is the surface stress induced by the adsorption; $F = \sigma b$ and $M_b = \sigma bh / 2$ are the concentrated load and moment exerted at the beam free end, respectively. (c) The distributed load modeling: s = F / L = $\sigma b / L$ and $M_b = \sigma bh / (2L)$ are the uniformly distributed load and moment along the length direction, respectively. Adapted from Ref. [4].

using the shifts of two resonant frequencies to uniquely determine the mass and surface stress induced by adsorption.

Figure 7.3(a) is a schematic of a cantilever with a uniform layer of adsorption on its upper surface. Figure 7.3(b) is a schematic of the concentrated load modeling, in which a concentrated load F and a concentrated moment M_b are applied at the cantilever free end. For brevity, the governing equation of the concentrated load modeling and the boundary conditions are given as follows [47–49]:

$$(m + \Delta m)\frac{\partial^2 w}{\partial t^2} + c\frac{\partial w}{\partial t} + E^* I \frac{\partial^4 w}{\partial x^4} - F\frac{\partial^2 w}{\partial x^2} = 0 \qquad (7.4)$$

where m is the beam mass per unit length, and Δm is the adsorption mass per unit length, which is assumed to have a uniform distribution all over the cantilever and is thus treated as a constant. In the applications of chemical and biological sensors, an adsorbed mass spanning the entire cantilever surface is preferred instead of an adsorbed at a selected area [50], which prevents the need for selective activation of surface and avoids unspecific binding. w is the beam deflection, and c is damping. E^*I is the beam bending stiffness. The concentrated load $F = \sigma b$ (σ is the adsorption induced surface stress, and b is the beam width) [47]. Clearly, in Eq. (7.4), one of the surface effects is modeled as an axial force (F), which can influence the resonant frequencies of the beam. The Stoney formula of Eq. (7.1) is to model the surface stress as a concentrated moment applied at the beam free end [47], which will not result in any resonant frequency change [4]. There are still some debates on how to model the surface stress. Besides the aforementioned Stoney formula and concentrated load modeling, there is following one called the distributed load modeling [4,47]:

$$(m + \Delta m)\frac{\partial^2 w}{\partial t^2} + c\frac{\partial w}{\partial t} + E^\star I \frac{\partial^4 w}{\partial x^4} - s(L - x)\frac{\partial^2 w}{\partial x^2} + s\frac{\partial w}{\partial x} = 0 \qquad (7.5)$$

where $s = F / L = \sigma b / L$ is the distributed load as shown in Figure 7.3(c), and L is the beam length. As the experiments show that the surface stress is directly related with the coverage density of adsorbate [5] or areal density of ligand–receptor binding [6], Zhang et al. [47] and Finot et al. [51] argued that surface stress should be viewed as the sum of two contributions: one is an axial force per unit length, and the other is a moment per unit cross section. In Ref. [4], the distributed load model of Eq. (7.5) is used. However, the inverse problem solving technique presented in Ref. [4] can also be applied to the concentrated load model of Eq. (7.4).

By introducing $\xi = x / L$, $W = w / L$, and $\tau = \sqrt{E^\star I / (mL^4)}\,t$, Eq. (7.5) has the following dimensionless form [4]:

$$(1 + a)\frac{\partial^2 W}{\partial \tau^2} + C\frac{\partial W}{\partial \tau} + \frac{\partial^4 W}{\partial \xi^4} - \Lambda(1 - \xi)\frac{\partial^2 W}{\partial \xi^2} + \Lambda\frac{\partial W}{\partial \xi} = 0 \qquad (7.6)$$

where $a = \dfrac{\Delta m}{m}$, $C = c\sqrt{\dfrac{L^4}{E^\star I m}}$, $\Lambda = \dfrac{\sigma b L^2}{E^\star I}$. Clearly, a indicates the ratio of the adsorption mass to the beam mass, and Λ indicates the ratios of the surface stress to the beam stiffness per unit width. C is the dimensionless damping. Again, in the real sensor application, a and Λ are unknown; the resonant frequencies are extracted from the beam frequency response curves [41]. Therefore, using the resonant frequencies (shifts) to determine a and Λ forms an inverse problem. For a given $(a, \Lambda) = (10^{-3}, 10^{-2})$, the first two resonant frequencies can be calculated from Eq. (7.6) as a direct problem as $\omega_1 = 3.516491$ and $\omega_2 = 22.025444$. Now, how to use these two (measured) resonant frequencies to determine a and Λ is presented in Figure 7.4.

Figure 7.4(a) plots the variation of the first eigenfrequency, ω_1, as a function of Λ and a, which is a titled plane. ω_1 increases monotonically with the increase of Λ and decreases monotonically with the increase of a. The level plane is the one with the fixed first eigenfrequency value of $\omega_1 = 3.516491$. The intersection of these two planes is all the combinations of Λ and a, which result in the same first eigenfrequency of $\omega_1 = 3.516491$. The intersection is a line marked in Figure 7.4(a). This line also indicates that the combinations resulting in a same eigenfrequency are infinite. Figure 7.4(b) plots the second eigenfrequency of ω_2 as a function of Λ and a. The level plane is the one with the fixed value of $\omega_2 = 22.025444$. Again, the intersection line of the two planes indicates the combinations of Λ and a resulting in $\omega_2 = 24.628$. Clearly, for any given values of Λ and a, each eigenfrequency is uniquely determined by Eq. (7.6). As an inverse problem, there are infinite combinations of Λ and a for a given eigenfrequency. However, as shown in Figure 7.4(c), for two given eigenfrequencies, their combinations of Λ and a, which are two lines, intersect. Physically, this intersection is used to uniquely determine the combination of Λ and a. In Figure 7.4(c), the intersection of the combinations of Λ and a for $\omega_1 = 3.516491$ and $\omega_2 = 22.025444$ is marked as a circle, which happens to be exactly $(a, \Lambda) = (10^{-3}, 10^{-2})$. Physically, that the inverse problem can be solved is due to
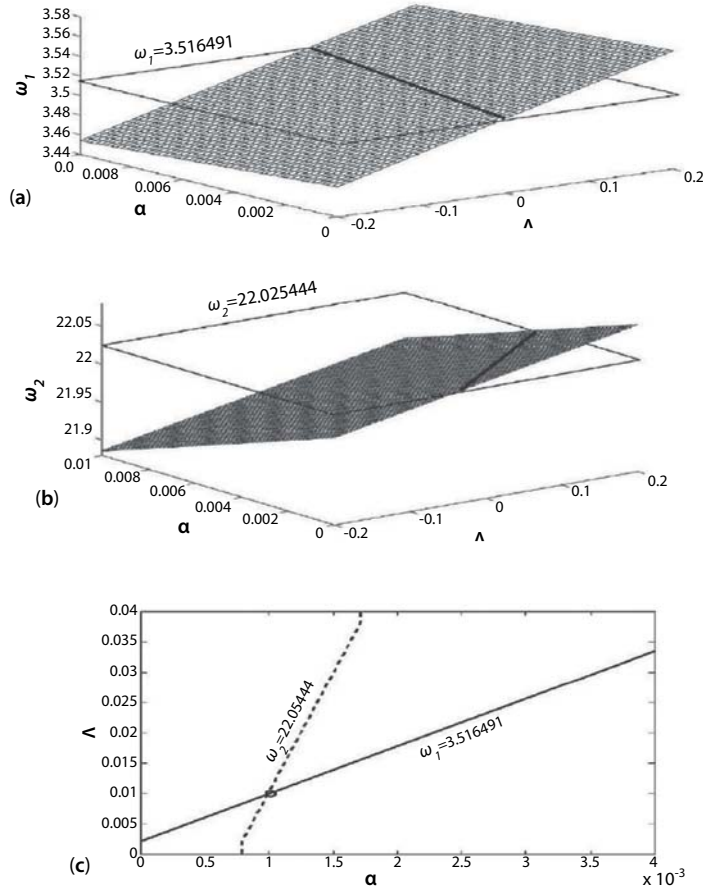
Figure 7.4 (a) Variation of the first resonance frequency (ω_1) as a function of α and Λ. The level plane is the one with a fixed resonance frequency of $\omega_1 = 3.516491$. The intersection of the two planes is marked with a solid line. (b) Variation of the second resonance frequency (ω_2) as a function of α and Λ. The level plane is the one with a fixed resonance frequency of $\omega_2 = 22.025444$. The intersection of the two planes is marked with a solid line. (c) The combinations of α and Λ for the resonant frequencies of $\omega_1 = 3.516491$ and $\omega_2 = 22.025444$, which are two lines marked in Figures 7.3 and 7.4. The intersection is marked with a circle, which corresponds to $(\alpha, \Lambda) = (10^{-3}, 10^{-2})$. Adapted from Ref. [4]

the fact that surface stress and mass have different impacts on the resonant frequencies, which is also reflected mathematically in Eq. (7.6). Here, the inverse problem is solved by using the first two resonant frequencies. As a higher resonant frequency has a higher sensitivity, the method can be easily extended to this application scenario by choosing to calculate two other different resonant frequencies in Eq. (7.6).

7.2.3   Determining the Surface Elasticity and Surface Stress by Measuring the Shifts of Resonant Frequencies

One of the motivations to solve the inverse problem of using the shifts of resonant frequency to determine surface elasticity and surface stress is ascribed to a debate in 1970s

[17]. In 1975, Lagowski *et al.* [52] found that the resonant frequencies of a microcantilever deviate significantly from those predicated by the axial load-free beam theory; they proposed that surface stress is the mechanism causing the resonant frequencies shifts. Subsequently, Gurtin *et al.* [53] disputed Lagowski's explanation; they argued that the resonant frequency is independent of surface stress and surface elasticity is the only mechanism responsible for the resonant frequency shifts. Lagowski's essential argument is that surface stress behaves as residual stress, which has the axial load effect and thus changes the resonant frequencies [52]; Gurtin's argument is that as the surface stress is induced inside a surface layer, there will be a corresponding force generated inside bulk due to constraint [53]. According to Newton's third law, the force inside the bulk has the same magnitude but opposite direction as the product of surface stress and the thickness of surface layer. Therefore, the total amount of the axial load inside a micro/nanostructure is zero, and the resonant frequencies are independent of surface stress, which is the same scenario of the bending of a bimetallic beam due to temperature studied by Timoshenko [54]. The application of ansatz that nanostructure=bulk + surface [55] in continuum mechanics leads to the so-called core–shell model [56–58], in which the core is bulk and the shell is surface layer. In a surface layer, the total surface stress (τ) is given as follows [56–58]:

$$\tau = \sigma + C_s \varepsilon \qquad (7.7)$$

where ε is the dimensionless strain, and C_s is the surface modulus. Here, τ is the result of charge redistribution as the electrons response to the effects of terminating a solid at a surface [59]. By the thermodynamics definition, τ is a tensor associated with the reversible work to elastically stretch a pre-existing surface [60]. We find that τ consists of two parts: σ and $C_s\varepsilon$; σ, which is strain independent, is often referred to as surface stress [52]; $C_s\varepsilon$, which is strain dependent, is often referred to as surface elasticity [53]. Surface elasticity is due to the formation of surface layer which has a different elastic property from that of a bulk [58,61]. Surface relaxation [61] and sometimes surface reconstruction [59] are the two profound mechanisms responsible for the formation of a surface layer. Both σ and C_s have the unit of force per unit length (Nm^{-1}) compared with that of force per unit area (Nm^{-2}) for the bulk stress and modulus. Here, σ and C_s can be either positive or negative [55], which can thus either stiffen or soften a micro/nanostructure. In dynamics, the effect of the structure stiffness change (either stiffening or softening) is embodied in the shifts of the structure resonant frequencies.

Lagowski *et al.* [52] and McFarland *et al.* [62] found surface stress by measuring the shifts of one resonant frequency and by assuming zero surface elasticity. Similarly, Gurtin *et al.* [53] found surface elasticity by proving that surface stress has no impact on the resonant frequency. Gavan *et al.* [63] are the first to use the two resonant frequencies of a microcantilever to determine the effects of surface elasticity and surface stress. Again, Gavan *et al.* [63] extracted the fitting value of surface stress/surface elasticity by assuming that of surface elasticity/surface stress to be zero, which excludes the general case that both surface elasticity and surface stress are non-zero [55]. Recently, many theoretical investigations [64–66] show that both surface elasticity and surface stress have the impact on the structure stiffness; however, the effect of surface elasticity is too small to explain the experimental observations for a slender structure. The reason

is geometrical, as shown in Ref. [17], the surface stress effect is amplified by a factor of $(L / D)^2$ (L and D are the length and diameter of a cylinder-like nanowire, respectively). For slender structure, because this $(L / D)^2$ factor is large, the surface stress effect is dominant if σ and C_s have the same order of magnitude [17]. However, for chunky structure or some materials whose C_s is significantly larger than σ, the surface elasticity effect must be considered [17]. Atomistic simulation is often used to obtain σ and C_s, which are determined by the underlying lattice structure and interatomic potential [55,67,68]. It is noted that σ and C_s calculated by atomistic simulation can be significantly different for the same material depending on what kind of interatomic potential is taken during the computation [17]. According to Song *et al.* [69], there is no experimental method that can determine both non-zero surface elasticity and surface stress at the same time. The goal of Ref. [17] is twofold: by solving the inverse problem, it provides (1) a viable experimental scheme to determine both non-zero surface elasticity and surface stress by measuring two (arbitrary) resonant frequencies; (2) an alternative method/theory other than atomistic simulation.

Actually, solving the inverse problem is very similar to the one of using the shifts of two resonant frequencies to determine the mass and surface stress [4] as presented in the last section. Here, we outline the procedures. The dimensionless governing equation is given as follows:

$$(1+\Delta)\frac{\partial^4 W}{\partial \xi^4} - N(1-\xi)\frac{\partial^2 W}{\partial \xi^2} + N\frac{\partial W}{\partial \xi} + \frac{\partial^2 W}{\partial \tau^2} = 0 \qquad (7.8)$$

where dimensionless parameters Δ and N indicate the effect s of surface elasticity and surface stress, respectively. Eq. (7.8) is similar to Eq. (7.6). The same inverse problem solving technique is applied: finding the all possible combinations of Δ and N for two given resonant frequencies and then find the intersection of these two infinite combinations, which uniquely determine Δ and N [17]. Again, this technique works. The physical reason is that surface elasticity and surface stress have different impacts on different resonant frequency [17].

Finally, we give our comment on the debate between Lagowski *et al.* [52] and Gurtin *et al.* [53] on whether surface stress can induce the stiffness/resonant frequency change. We are prone to the opinion that surface stress should be viewed as residual stress [70,71]. The experiment by Chen *et al.* [72] shows that an adsorbate can significantly increase the resonant frequencies of a monolayer graphene resonator. For a monolayer graphene, there is no room to form a surface layer which has a different mechanical property. Chen *et al.* [72] ascribed the increase of resonant frequencies as the adsorption-induced tension, which in essence is also surface stress. The atomistic simulations [73,74] also show that adsorption can induce electronic and mechanical distortion of a graphene structure. The adsorption-induced distortion, which is responsible for the presence of surface stress, is similar to the doping in semiconductor materials. The doped impurities inside a semiconductor material distort its lattice structure, which makes residual stress prevalent in many MEMS devices [75,76]. For the argument of the Newton third law to apply for a bi-material composite case, the ideal interface condition is (implicitly) assumed. In an ideal interface, the interface has no zero thickness, and displacement/strain is continuous across the interface [54]. However,

in reality, the interface is non-ideal or say, flawed, which has finite thickness and slips. The interfacial slip causes the discontinuity of displacement/strain at the interface and this non-ideal interface effect amplifies with the decreasing dimension of a structure [77–79]. Here, the essential idea is that for a micro/nano bi-material composite structure, Newton's third law does not apply for the two layers, which means that the force inside one layer does not has the same magnitude but the opposite direction as that of the other layer. In a micro/nano "bi-material" composite structure, the correct modeling should be three layers, i.e., layer 1–interface–layer 2 [77,79]. Of course, we have no intention to challenge Newton's third law; it still applies between layer 1 and interface, and between layer 2 and interface [77,79], but NOT between layer 1 and layer 2. Quite often, defects such as dislocation, twin and cavity are localized and accumulate at an interface [77,80], which makes the stress around the interface very high. The stressed state of a micro/nanostructure is balanced externally as a whole through boundaries, which equivalently adds the axial load or bending moment on the micro/nanostructure [75,76]. And, the axial load is responsible for the structural stiffness change [4,17].

7.2.4   Determining the Stiffness and Mass of Biochemical Adsorbates by a Resonator Sensor

Surface stress is an effective sensing mechanism for many receptor-based sensors [5,6]. However, the receptor–ligand binding is highly selective for identifying an adsorbate/ligand; the challenges for developing robust and stable recognition methods through functionalized coatings (i.e., the receptor materials) and even interpreting the responses of receptor-based sensor still remain [9]. The development for the receptorless or receptor-free sensors, which bypass the chemistry of receptor–ligand binding and capitalize on the intrinsic material properties of adsorbate, has been called for [9]. The mass density (related with mass) and Young's modulus (related with stiffness) are the intrinsic material properties, which can be used to identify the material of an adsorbate. Solving the inverse problem of using resonant frequencies to determine the stiffness and mass of adsorbates can provide an alternative method of mass identification. The mass information only is insufficient to provide fundamental insights into the resonator-based molecular detection [81]. In general, the appropriate properties of a detected material including its mechanical properties as well as the mass must be considered when interpreting the resonator data [82]. The adsorption tests of *E. coli* bacteria on a silicon resonator by Ramos *et al.* [14,15] show that the system resonant frequencies increase. According to Eq. (7.2), the mass addition due to adsorption can only decrease the resonant frequency. At same time, the surface of resonator is not functionalized and surface stress is thus very small because of the high selectivity as discussed earlier [14,15]. The increase of resonant frequency can only mean that the stiffness of the bacteria plays a more important or even a dominant role [14,15].

In the experiment [14,15], the shifts of resonant frequencies are recorded. To solve the inverse problem, Ramos *et al.* [14] counted the total *E. coli* bacteria number (about 4200) and calculated the mass; the bacteria stiffness was then obtained by curve-fitting, which is a laborious work. They changed the adsorption location to try to "uncouple" the effects of stiffness and mass of the bacteria [14]. Our study [83] shows that the methods including shifting adsorption location, multiple resonant frequencies, and

changing the adsorption length cannot be used to solve the inverse problem. By varying the adsorbate thickness and utilizing a geometric approximation, a solution method to the inverse problem can be presented [83]. Here, we have a brief discussion on why the multiple resonant frequencies method, which solves the two inverse problems [4,17] as presented above, cannot work for this inverse problem. When the resonator surface is fully covered by an adsorbate layer, the (circular) resonant frequency is given as follows [83]:

$$\omega_i = \sqrt{\frac{1+\alpha}{1+\beta}}\omega_i^o \qquad (7.9)$$

where ω_i is the ith resonant frequency with the presence of an adsorbate layer, and ω_i^o is the ith resonant frequency with no adsorbate layer. The dimensionless parameters α and β indicate the effects of the stiffness and mass of an adsorbate layer, respectively [83]. It is worth pointing out that Eq. (7.9) applies to all resonant frequencies, which is somewhat surprising and this is also the exact reason why the multiple resonant frequencies method cannot work. According to Eq. (7.9) for the full coverage scenario, no matter how many ω_i are measured, they all lead to the same one equation of Eq. (7.9) and mathematically, two unknown variables (α and β) cannot be solved by one equation. By varying the thickness of adsorbate layer, two independent equations can be derived from Eq. (7.9), from which α and β can be solved. Therefore, the inverse problem-solving method [83] requires to measure the thickness of adsorbate layer. However, the thickness measurement is much easier than that of stiffness (Young's modulus) or mass. For example, the adsorbate layer thickness of alkanethiol [5] and DNA [6] was measured by ellipsometry; the thickness of a membrane protein (FhuA) [84] and gold film [85] was measured by atomic force microscope (AFM). It can be even much simpler in a well-controlled inkjetting deposition procedure, in which the volume and spreading shape/area are precisely controlled/monitored [86] and the thickness can thus be easily calculated. Once α and β are solved, the mass density and Young's modulus of an adsorbate layer can be readily found out by a simple relation [83], which can be used to identify the material of adsorbate.

7.3 Inverse Problems in the MEMS Stiction Test

Suspended micromechanical structures are extensively used in varieties of microsensors and microactuators. In general, it is desirable to make sensors and actuators that have a minimum gap distance and a large surface area [87]. Smaller gap distance requires smaller actuation voltage, less power consumption, and less amount of energy stored in the system. If the stored energy is large, the discharge current densities during the contact of suspended structure and substrate can be so large to ablate the active element or damage the electrode, which is the so-called burn-out phenomenon [88]. A straightforward solution to burn out is the smaller gap distance. However, such solution comes at the expense of favoring the stiction failure mode. Use of dimples or cavities [87] to reduce contact area, or hydrophobic surface coating to reduce surface energy [88], or to operate the device in dry or vacuum environment to reduce capillary force,

can not completely prevent stiction from occurring because of the presence of van der Waals (vdW) force [89].

Stiction is a major failure mechanism for the MEMS structures, and extensive studies have been done on this topic. Stiction is the competition result of the microstructure elastic energy and microstructure–substrate interfacial energy, i.e., the work of adhesion or say, adhesion energy [19–23]. The presence of residual stress and its gradients in a microstructure, which in essence changes the stiffness and elastic energy of the microstructure [75,76], is a common phenomenon. As a direct outgrowth of silicon-based microelectronics, the manufacturing technique of using successively patterned deposition of thin-film polysilicon and sacrificial oxide layers is applied to fabricate those MEMS structures [24]. Polysilicon is prone to have residual stress/gradients, which is strongly dependent on the deposition process and heating cycles, including doping or annealing [90]. For a clamped–clamped microstructure [19–23], the axial thermoelastic stress due to the temperature variation also has the impact on the microstructure stiction [90]. Even for a cantilever, when the stiction occurs with the S-shape configuration, which in essence is also a clamped–clamped configuration [20,22,24], thermoelastic stress is also shown to have an influence on the microstructure stiction [91]. Residual stress can be the dominant factor in the microstructure deflection and stiction [92]. The previous studies on the stiction of a microstructure either assume the zero residual stress [19–24,93], or the residual/thermoelastic stress is known as a measured quantity [91,92], or a control parameter [94]. However, residual stress/gradients and thermoelastic stress in general are not known *a priori*. Thermoelastic stress is obtained by measuring the material coefficient of thermal expansion (CTE) and the temperature variation [90,91]. When the residual stress gradients are asymmetric along the microstructure thickness, which generates bending moment and thus deflection, the residual stress and its gradients can be characterized as a function of the microstructure dimensions [75,76]. By any standard, measuring the residual stress and its gradients or thermoelastic stress inside a microstructure is not a trivial thing. Extra experimental setup to monitor the temperature variation and heating devices are often needed in the thermoelastic stress measurement [91]. Multiple special specimens are needed; the extraction of residual stress and its gradients often involves complex numerical simulation [75,76]. Besides the residual stress/gradients and thermoelastic stress, the nominal adhesion energy is another unknown material property in a stiction test. The nominal adhesion energy is found by minimizing the system total energy with respect to the suspension length [19–24,87,90,93]. The total energy is the sum of the elastic energy and surface energy. The residual stress and thermoelastic stress generate axial force; the residual stress gradients generate bending moment. They all result in the change of the microstructure elastic energy. When the residual stress/gradients and thermoelastic stress are (assumed) zero or measured, the elastic energy can be calculated and the total energy minimization gives the relation of adhesion energy and detachment length. Such relation is given as follows for a cantilever beam with zero axial stress:

$$\gamma_s = C \frac{EH^2 t^3}{S^4} \tag{7.10}$$

where γ_s is the nominal adhesion energy, E and t are the beam Young's modulus and thickness, respectively. H is the gap distance; S is called the suspension length or the detachment length. C is a constant, $C = 3/8$ for the arc-shaped stiction [21] and $C = 3/2$ for the S-shaped stiction [24]. Clearly, Eq. (7.10) presents a one-to-one relationship of adhesion energy and suspension length: once the suspension length is measured, the adhesion energy is uniquely determined. Similarly, if the non-zero residual axial stress/strain is measured, the adhesion energy can also be uniquely determined by the suspension length [90]. When the axial stress is unknown, as shown in this study, the one-to-one relationship can no longer hold: there are infinite combinations of the axial stress and adhesion energy which can result in the same suspension length. Here, the inverse problem is encountered as: *How to use the stiction shape to determine the axial stress and adhesion energy?*

The arc- and S-shapes of stiction are shown in Figure 7.5. Eq. (7.10) actually does not tell us how to choose between these two shapes and only the following vague rule applies: generally speaking, slender beam forms an S-shape, and its unstuck/suspension length is appreciably shorter than the beam length; chunky beam forms an arc-shape, and its unstuck/suspension length is approximately equal to the beam length. The arc- and S-shapes are the assumed deflection shapes [22,23,95]. The contact mechanics model [22,95] shows that when axial load is zero, S-shape indeed is a very good approximation shape for the stiction shape of a slender beam; arc-shape is an idealized one which deviates significantly from that of a chunky beam. The contact mechanics model [22,95] also shows that Eq. (7.10) can result in the significant error on the evaluation of adhesion energy. As listed in Ref. [22], the difference of the measured adhesion energy for polysilicon in the stiction tests using Eq. (7.10) is more than one thousand times. Hariri *et al.* [96] commented that "the inconsistency and unreliability of the experimental data" are the main deficiencies of those experiments; some of data are even observed to be in contradiction with one another. More explicitly, van Spengen *et al.* [97] concluded that "the surface interaction energy measurement using stuck beams needs considerable research before we can conclude anything definite about the precise magnitude of the measured surface interaction energy". Adhesion energy can be measured other than
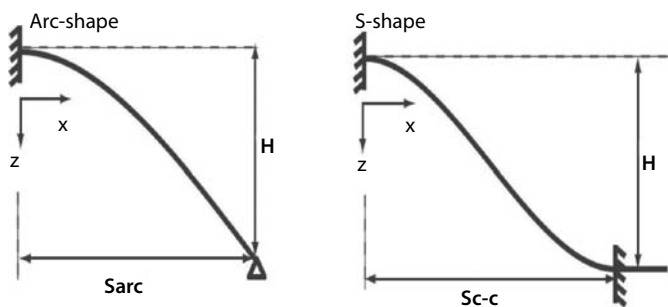
Figure 7.5 Schematics of arc-shape and S-shape stiction. For arc-shape, the boundary conditions are the clamped–hinged ones; for S-shape, the boundary conditions are the clamped–clamped ones. Adapted from Refs. [22,23].

the stiction test, for example, the measurement of the pull-off force [98,99]. However, it is extremely difficult to exert a pull-off force on a suspended MEMS device. The goal of the contact mechanics model [22,95] is to improve the evaluation on adhesion energy on the modeling aspect. Ref. [23] adopts the contact mechanics model [22,95] to solve the inverse problem. Furthermore, the axial load effect can be easily implemented in the contact mechanics model [23]. In contrast, arc- and S-shapes are for the zero axial load scenario, and they deviate significantly when axial load is large [23]. In stiction test, the mature measurement technique of Michelson interferometer is often used [22,24, 100], and the out-of-plane deflection of a stuck microstructure can be measured with the high accuracy of nanometer scale [100]. The deflection profile of a stuck microbeam is used to identify the structural nonidealties such as the compliance of support post [89,100]. Ref. [23] is to use the deflection profile to determine the axial stress and adhesion energy. To be more specific, two parameters are taken from the deflection profile, which are the suspension length and rise above substrate (at a given location) [23]. The axial stress and adhesion energy determine the stiction shape. For a given suspension length or rise, there are infinite combinations of the axial stress and adhesion energy. However, when the suspension length and rise are both given, the axial stress and adhesion energy are uniquely determined.

Acknowledgment

References

1. G. Anger, *Inverse Problems in Differential Equations*, Plenum Press, New York, 1990.
2. T.P. Burg and S.R. Manalis, *Appl. Phys. Lett.*, Vol. 83, 2698–2700, 2003.
3. T.P. Burg, M. Godin, S.M. Knudsen, W. Shen, G. Carlson, J.S. Foster, K. Babcock, and S.R. Manalis, *Nature*, Vol. 446, 1066–1069, 2007.
4. Y. Zhang, *Sens. Actuator A-Phys.*, Vol. 194, 169–175, 2013.
5. R. Berger, E. Delamarche, H.P. Lang, Ch. Gerber, J.K. Gimzewski, E. Meyer, and H.J. Guntherodt, *Science*, Vol. 276, 2021–2024, 1997.
6. J. Fritz, M.K. Baller, H.P. Lang, H. Rothuizen, P. Vettiger, E. Meyer, H.J. Guntherodt, Ch. Gerber, and J.K. Gimzewski, *Science*, Vol. 288, 316–318, 2000.
7. N.V. Lavrik, M.J. Sepaniak, and P.G. Datskos, *Rev. Sci. Instrum.* Vol. 75, 2229–2253, 2004.
8. S.T. Koev, M.A. Powers, H. Yi, L.Q. Wu, W.E. Bentley, G.W. Rubloff, G.F. Payne, and R. Ghodssi, *Lab. Chip*, Vol. 7, 103–111, 2007.
9. R.H. Farahi, A. Passian, L. Tetard, and T. Thundat, *ACS Nano.*, Vol. 6, 4548–4556, 2012.
10. L. Meirovitch, *Analytical Methods in Vibrations*, Prentice Hall, New York, 1967.
11. M.S. Hanay, S. Kelber, A.K. Naik, D. Chi, S. Hentz, E.C. Bullard, E. Colinet, L. Duraffourg and M.L. Roukes, *Nat. Nanotechnol.*, Vol. 7, 602–608, 2012.
12. K. Jensen, K. Kim, and A. Zettl, *Nat. Nanotechnol.*, Vol. 3, 533–537, 2008.
13. J. Chaste, A. Eichler, J. Moser, G. Ceballos, R. Rurali, and A. Bachtold, *Nat. Nanotechnol.*, Vol. 7, 301–304, 2012.

14. D. Ramos, J. Tamayo, J. Mertens, M. Calleja, and A. Zaballos, *J. Appl. Phys.*, Vol. 100, 106105, 2006.

15. J. Tamayo, D. Ramos, J. Mertens, and M. Calleja, *Appl. Phys. Lett.*, Vol. 89, 224104, 2006.

16. S. Cherian and T. Thundat, *Appl. Phys. Lett.*, Vol. 80, 2219–2221, 2002.

17. Y. Zhang, L. Zhuo, and H. Zhao, *Proc. R. Soc. A*, Vol. 469, 20130449, 2013.

18. P. Mohanty, D.A. Harrington, K.L. Ekinci, Y.T. Yang, M.J. Murphy, and M.L. Roukes, *Phys. Rev. B*, Vol. 66, 085416, 2002.

19. R. Legtenberg, T. Tilmans, J. Elders, and M. Elwenspoek, *Sens. Actuat. A Phys.*, Vol. 43, 230–238, 1994

20. C.H. Mastrangelo and C.H. Hsu, *J. Microelectromech. Syst.*, Vol. 2, 33–43, 1993.

21. C.H. Mastrangelo and C.H. Hsu, *J. Microelectromech. Syst.*, Vol. 2, 44–55, 1993.

22. Y. Zhang and Y.P. Zhao, *Int. J. Solids Struct.*, Vol. 49, 2203–2214, 2012.

23. Y. Zhang and Y.P. Zhao, *Microsyst. Technol.*, 2014 (DOI: 10.1007/s00542-014-2127-6).

24. M.P. de Boer and T.A. Michalske, *J. Appl. Phys.*, Vol. 86, 817–827, 1999.

25. M.P. de Boer, J.A. Knapp, T.M. Mayer, and T.A. Michalske, "The role of interfacial properties on MEMS performance and reliability", in: C. Gorecki, eds., *Microsystems Metrology and Inspection*, Spie-Int Soc, Optical Engineering, Bellingham, pp. 2–15, 1999.

26. A.K. Naik, M.S. Hanay, W.K. Hiebert, X.L. Feng, and M.L. Roukes, *Nat. Nanotechnol.*, Vol. 4, 445–450, 2009.

27. K.L. Ekinci, Y.T. Yang, and M.L. Roukes, *J. Appl. Phys.*, Vol. 95, 2682–2689, 2004.

28. Y. Zhang and Y.P. Zhao, *Proc. R. Soc. A*, Vol. 470, 2014.

29. R.G. Knobel, *Nat. Nanotechnol.*, Vol. 3, 525–526, 2008.

30. X. Huang, C.A. Zorman, M. Mehregany, and M.L. Roukes, *Nature*, Vol. 421, 496–496, 2003.

31. J.S. Bunch, A.M. van der Zande, S.S. Verbridge, I.W. Frank, D.M. Tanenbaum, J.M. Parpia, H.G. Craighead, and P.L. McEuen, *Science*, Vol. 315, 490–493, 2007.

32. A. Eichler, J. Moser, J. Chaste, M. Zdrojek, I. Wilson-Rae, and A. Bachtold, *Nat. Nanotechnol.*, Vol. 6, 339–342, 2011.

33. S.Y. Kim and H. Park, *Nanotechnology*, Vol. 21, 105710, 2010.

34. A. Jockel, M.R. Rakher, M. Korppi, S. Camerer, D. Hunger, M. Mader, and P. Treutlein, *Appl. Phys. Lett.*, Vol. 99, 143109, 2011.

35. X. Xia and X. Li, *Rev. Sci. Instr.*, Vol. 79, 074301, 2008.

36. F. Schedin, A.K. Geim, S.V. Morozov, E.W. Hill, P. Blake, M.I. Katsnelson, and K.S. Novoselov, *Nat. Mater.*, Vol. 6, 652–655, 2007.

37. W.H. Grover, A.K. Bryan, M. Diez-Silva, S. Suresh, J.M. Higgins, and S.R. Manalis, *Proc. Natl. Acad. Sci. USA*, Vol. 108, 10992–10996, 2011.

38. A. Gupta, D. Akin, and R. Bashir, *Appl. Phys. Lett.*, Vol. 84, 1976–1978, 2004.

39. S. Dohn, R. Sandberg, W. Svendsen, and A. Boisen, *Appl. Phys. Lett.*, Vol. 86, 233501, 2005.

40. S. Dohn, W. Svendsen, A. Boisen, and O. Hansen, *Rev. Sci. Instr.*, Vol. 78, 103303, 2007.

41. G.Y. Chen, T. Thundat, E.A. Wachter, and R.J. Warmack, *J. Appl. Phys.*, Vol. 77, 3618–3622, 1995.

42. T. Thundat and L. Maya, *Surf. Sci.*, Vol. 430, L546–L552, 1999.

43. A.W. McFarland, M.A. Poggi, L.A. Bottomley, and J.S. Colton, *J. Micromech. Microengr.*, Vol. 15, 785–791, 2005.

44. F.M. Battiston, J.P. Ramseyer, H.P. Lang, M.K. Baller, Ch. Gerber, J.K. Gimzewski, E. Meyer, and H.J. Guntherodt, *Sens. Actuat. B Chem.*, Vol. 77, 122–131, 2001.

45. K.L. Ekinci and M.L. Roukes, *Rev. Sci. Instrum.*, Vol. 76, 061101, 2005.

46. R. Merkel, P. Nassoy, A. Leung, K. Ritchie, and E. Evans, *Nature*, Vol. 397, 50–53, 1999.

47. Y. Zhang, Q. Ren, and Y.P. Zhao, *J. Phys. D Appl. Phys.*, Vol. 37, 2140–2145, 2004.

48. J. Dorignac, A. Kalinowski, S. Erramilli, and P. Mohanty, *Phys. Rev. Lett.*, Vol. 96, 186105, 2006.
49. Q. Ren and Y.P. Zhao, *Microsyst. Technol.*, Vol. 10, 307–314, 2004.
50. M.K. Ghatkesar, V. Barwich, T. Braun, J. Ramseyer, Ch. Gerber, M. Hegner, H.P. Lang, U. Drechsler, and M. Despont, *Nanotechnology*, Vol. 18, 445502, 2007.
51. E. Finot, A. Passian, and T. Thundat, *Sensors*, Vol. 8, 3497–3541, 2008.
52. J. Lagowski, H.C. Gatos, and E.S. Sproles, *Appl. Phys. Lett.*, Vol. 26, 493–495, 1975.
53. M.E. Gurtin, X. Markenscoff, and R.N. Thurston, *Appl. Phys. Lett.*, Vol. 29, 529–530, 1976.
54. S. Timoshenko, *J. Opt. Soc. Am.*, Vol. 11, 233–255, 1925.
55. V.B. Shenoy, *Phys. Rev. B*, Vol. 71, 094104, 2005.
56. P. Lu, H.P. Lee, C. Lu, and S.J. O'Shea, *Phys. Rev. B*, Vol. 72, 085405, 2005.
57. J. He and C.M. Lilley, *Appl. Phys. Lett.*, Vol. 93, 263108, 2008.
58. J. He and C.M. Lilley, *Nano Lett.*, Vol. 8, 1798–1802, 2008.
59. H. Ibach, *Surf. Sci. Rep.*, Vol. 29, 193–263, 1999.
60. R.C. Cammarata, K. Sieradzki, and F. Spaepen, *J. Appl. Phys.*, Vol. 87, 1227–1234, 2000.
61. J.G. Guo and Y.P. Zhao, *Nanotechnology*, Vol. 18, 295701, 2007.
62. A.W. McFarland, M.A. Poggi, M.J. Doyle, L.A. Bottomley, and J.S. Colton, *Appl. Phys. Lett.*, Vol. 85, 053505, 2005.
63. K.B. Gavan, H.J.R. Westra, E. van der Drift, W.J. Venstra, and H.S.J. van der Zant, *Appl. Phys. Lett.*, Vol. 94, 233108, 2009.
64. X. Yi and H.L. Duan, *J. Mech. Phys. Solids*, Vol. 57, 1254–1266, 2009.
65. H.L. Duan, *Acta Mech. Solida Sin.*, Vol. 23, 1–11, 2010.
66. D.W. Dareing and T. Thundat, *J. Appl. Phys.*, Vol. 97, 043526, 2005.
67. H.S. Park and P.A. Klein, *J. Mech. Phys. Solids*, Vol. 56, 3144–3166, 2008.
68. W. Haiss, *Rep. Prog. Phys.*, Vol. 64, 591–648, 2001.
69. F. Song, G.L. Huang, H.S. Park, and X.N. Liu, *Int. J. Solids Struct.*, Vol. 48, 2154–2163, 2011.
70. Y. Li, B. Fang, J. Zhang, and J. Song, *J. Appl. Phys.*, Vol. 110, 114303, 2011.
71. Y. Li, J. Song, B. Fang, and J. Zhang, *J. Phys. D, Appl. Phys.*, Vol. 44, 425304, 2011.
72. C. Chen, S. Rosenblatt, K.I. Bolotin, W. Kalb, P. Kim, I. Kymissis, H.L. Stormer, T.F. Heinz, and J. Hone, *Nat. Nanotechnol.*, Vol.4, 861–867, 2009.
73. M. Chi and Y.P. Zhao, *Comput. Mater. Sci.*, Vol. 46, 1085–1090, 2009.
74. M. Chi and Y.P. Zhao, *Comput. Mater. Sci.*, Vol. 56, 79–84, 2012.
75. Y. Zhang, *J. Micromech. Microeng.*, Vol. 17, 753–762, 2007.
76. Y. Zhang and Y.P. Zhao, *Microsys. Technol.*, Vol. 12, 357–364, 2006.
77. Y. Zhang, *J. Appl. Mech.*, Vol. 75, 011008, 2008.
78. I.C. Noyan, C.E. Murray, J.S. Chey, and C.C. Goldsmith, *Appl. Phys. Lett.*, Vol. 85, 724–726, 2004.
79. C.E. Murray and I.C. Noyan, *Philos. Mag. A*, Vol. 82, 3087–3117, 2002.
80. Y. Zhang, *J. Mater. Sci.*, Vol. 43, 88–97, 2008.
81. K. Eom, H.S. Park, D.S. Yoon, and T. Kwon, *Phys. Rep.*, Vol. 503, 115–163, 2011.
82. H. Craighead, *Nat. Nanotechnol.*, Vol. 2, 18–19, 2007.
83. Y. Zhang. *Sens. Actuat. B Chem.*, Vol. 202, 286–293, 2014.
84. T. Braun, M.K. Ghatkesar, N. Backmann, W. Grange, P. Boulanger, L. Letellier, H.P. Lang, A. Bietsch, Ch. Gerber, and M. Hegner, *Nat. Nanotechnol.*, Vol. 4, 179–185, 2009.
85. D. Lee, S. Kim, N. Jung, T. Thundat, and S. Jeon, *Nanotechnology*, Vol. 106, 024310, 2009.
86. A. Bietsch, J. Zhang, M. Hegner, H.P. Lang, and Ch. Gerber, *Nanotechnology*, Vol. 15, 873–880, 2004.
87. F. Yang, *J. Appl. Phys.*, Vol. 100, 124511, 2006.
88. O.Y. Loh and H.D. Espinosa, *Nat. Nanotechnol.*, Vol. 7, 283–295, 2012.

89. F.W. Delrio, M.P. De Boer, J.A. Knapp, E.D. Reedy, P.J. Clews, and M.L. Dunn, *Nat. Mater.*, Vol. 4, 629–634, 2005.

90. Y. Yee, M. Park, and K. Chun, *J. Microelectromech. Syst.*, Vol. 7, 339–344, 1998.

91. J.W. Rogers, T.J. Mackin, and L.M. Phinney, *J. Microelectromech. Syst.*, Vol. 11, 512–520, 2002.

92. M.F. Wong, G. Duan, and K.T. Wan, *J. Appl. Phys.*, Vol. 101, 024903, 2007.

93. Y. Zhang and Y.P. Zhao, *Acta Mech. Solida Sin.*, Vol. 17, 104–112, 2004.

94. C.S. Majidi, R.E. Groff, and R.S. Fearing, *J. Appl. Phys.*, Vol. 98, 103521, 2005.

95. Y. Zhang and Y.P. Zhao, *Sens. Actuat. A Phys.*, Vol. 17, 381–390, 2011.

96. A. Hariri, J.W. Zu, and R. Ben Mrad, *J. Micromech. Microeng.*, Vol. 16, 1195–1206, 2006.

97. W.M. van Spengen, R. Puers, and I. De Wolf, *J. Micromech. Microeng.*, Vol. 12, 702–713, 2002.

98. Y. Zhang, *J. Adhes. Sci. Technol.*, Vol. 22, 699–715, 2008.

99. Y. Zhang, *J. Adhes. Sci. Technol.*, Vol. 25, 1435–1464, 2011.

100. B.D. Jensen, M.P. de Boer, N.D. Masters, F. Bitsie, and D.A. LaVan, *J. Microelectromech. Syst.*, Vol. 10, 336–346, 2001.